

Learning to Correct Overexposed and Underexposed Photos

Mahmoud Afifi^{1,2*}, Konstantinos G. Derpanis¹,
Björn Ommer³, and Michael S. Brown¹

¹Samsung AI Centre (SAIC), Toronto, Canada

²York University, Canada ³Heidelberg University, Germany

Abstract. Capturing photographs with wrong exposures remains a major source of errors in camera-based imaging. Exposure problems are categorized as either: (i) overexposed, where the camera exposure was too long, resulting in bright and washed-out image regions, or (ii) underexposed, where the exposure was too short, resulting in dark regions. Both under- and overexposure greatly reduce the contrast and visual appeal of an image. Prior work mainly focuses on underexposed images or general image enhancement. In contrast, our proposed method targets *both* over- and underexposure errors in photographs. We formulate the exposure correction problem as two main sub-problems: (i) color enhancement and (ii) detail enhancement. Accordingly, we propose a coarse-to-fine deep neural network (DNN) model, trainable in an end-to-end manner, that addresses each sub-problem separately. A key aspect of our solution is a new dataset of over 24,000 images exhibiting a range of exposure values with a corresponding properly exposed image. Our method achieves results on par with existing state-of-the-art methods on underexposed images and yields significant improvements for images suffering from overexposure errors.

Keywords: Deep learning, camera-based imaging, exposure correction, datasets

1 Introduction

The exposure used at capture time directly affects the overall brightness of the final rendered photograph. Digital cameras control exposure using three main factors: (i) capture shutter speed, (ii) f-number, which is the ratio of the focal length to the camera aperture diameter, and (iii) the ISO value to control the amplification factor of the received pixel signals. In photography, exposure settings are represented by exposure values (EVs), where each EV refers to different combinations of camera shutter speeds and f-numbers that result in the same exposure effect—also referred to as ‘equivalent exposures’ in photography.

Digital cameras can adjust the exposure value of captured images for the purpose of varying the brightness levels. This adjustment can be controlled manually

* This work was done while Mahmoud Afifi was an intern at the SAIC.



Fig. 1: The first column shows photographs with over- and underexposure errors. Results from current commercial software and the proposed method are shown.

by users or performed automatically in an auto-exposure (AE) mode. When AE is used, cameras adjust the EV to compensate for low/high levels of brightness in the captured scene using through-the-lens (TTL) metering that measures the amount of light received from the scene [1].

Exposure errors can occur due to several factors, such as errors in measurements of TTL metering, hard lighting conditions (e.g., very low lighting and backlighting), dramatic changes in the brightness level of the scene, or errors made by users in the manual mode. Such exposure errors are introduced early in the capture process and are thus hard to correct after rendering the final 8-bit image. This is due to the highly nonlinear operations applied by the camera image signal processor (ISP) afterwards to render the final 8-bit standard RGB (sRGB) image [2].

Fig. 1 shows typical examples of images with exposure errors. In Fig. 1, exposure errors result in either very bright image regions, due to overexposure, or very dark regions, caused by underexposure errors, in the final rendered images. Correcting images with such errors is a challenging task even for well-established image enhancement software packages as shown in Fig. 1. Although both over- and underexposure errors are common in photography, most prior work is mainly focused on correcting underexposure errors [3–7] or generic image quality enhancement [8, 9].

Contributions We propose a coarse-to-fine deep learning method for exposure error correction of *both* over- and underexposed sRGB images. Our approach formulates the exposure correction problem as two main sub-problems: (i) color and (ii) detail enhancement. We propose a coarse-to-fine deep neural network (DNN) model, trainable in an end-to-end manner, that begins by correcting the global color information and subsequently refines the image details. In addition to our DNN model, a key contribution to the exposure correction problem is a new dataset containing over 24,000 images rendered from raw-RGB to sRGB with different exposure settings. Each image in our dataset is provided with a corresponding properly exposed reference image. Lastly, we present an extensive set of evaluations and ablations of our proposed method with comparisons to the state of the art. We demonstrate that our method achieves results on par

with previous methods dedicated to underexposed images and yields significant improvements on overexposed images.

2 Related Work

The focus of our paper is on correcting exposure errors in camera-rendered 8-bit sRGB images. We refer the reader to [10–13] for representative examples for rendering linear raw-RGB images captured with low light or exposure errors. The related work is organized into three categories: (i) exposure error correction, (ii) high dynamic range (HDR) restoration and generic image enhancement, and (iii) related paired datasets.

Exposure Correction Traditional methods for exposure correction rely on image histograms to re-balance image intensity values aiming to correct exposure errors and enhance image contrast [14–18]. Alternatively, tone curve adjustment is used to correct images with exposure errors. This process is performed by relying either solely on input image information [19] or trained deep learning models [20, 21]. The majority of prior work adopts the Retinex theory [22] by assuming that improperly exposed images can be formulated as a pixel-wise multiplication of target images, captured with correct exposure settings, by illumination maps. Thus, the goal of these methods is to predict illumination maps to recover the well-exposed target images. Representative Retinex-based methods include [3, 4, 22–26] and the most recent deep learning ones [5–7]. Most of these methods, however, are restricted to correcting underexposure errors [3–7]. In contrast to the majority of prior work, our work is the first deep learning method to explicitly correct *both* overexposed and underexposed photographs.

HDR Restoration and Image Enhancement HDR restoration is the process of reconstructing scene radiance HDR values from one or more low dynamic range (LDR) input images. Prior work either requires access to multiple LDR images [27–29] or uses a single LDR input image, which is converted to an HDR image by hallucinating missing information [30, 31]. Ultimately, these reconstructed HDR images are mapped back to LDR for perceptual visualization. This mapping can be directly performed from the input multi-LDR images [32, 33], the reconstructed HDR image [34], or directly from the single input LDR image without the need for radiance HDR reconstruction [8, 9]. There are also methods that focus on general image enhancement that can be applied to enhancing images with poor exposure. In particular, work by [35, 36] was developed primarily to enhance images captured on smartphone cameras by mapping captured images to appear as high-quality images captured by a DSLR. Our work does not seek to reconstruct HDR images or general enhancement, but instead is trained to explicitly address exposure errors.

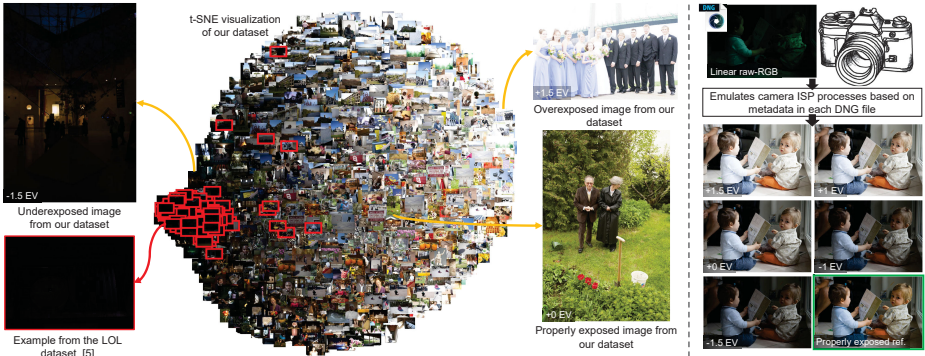


Fig. 2: Dataset overview. Our dataset contains images with different exposure error types and their corresponding properly exposed reference images. Shown is a t-SNE visualization [37] of all images in our dataset and the low-light (LOL) paired dataset (outlined in red) [5]. Notice that LOL covers a relatively small fraction of the possible exposure levels, as compared to our introduced dataset. Our dataset was rendered from linear raw-RGB images taken from the MIT-Adobe FiveK dataset [38]. Each image was rendered with different relative exposure values (EVs) by an accurate emulation of the camera ISP processes.

Paired Dataset Paired datasets are crucial for supervised learning for image enhancement tasks. Existing paired datasets for exposure correction focus only on low-light underexposed images. Representative examples include Wang et al.’s dataset [7] and the low-light (LOL) paired dataset [5]. Unlike existing datasets for exposure correction, we introduce a large image dataset rendered with a wide range of exposure errors. Fig. 2 shows a comparison between our dataset and the LOL dataset in terms of the number of images and the variety of exposure errors in each dataset. The LOL dataset covers a relatively small fraction of the possible exposure levels, as compared to our introduced dataset. Our dataset is based on the Adobe-MIT FiveK dataset [38] and is accurately rendered by adjusting the high tonal values provided in camera sensor raw-RGB images to realistically emulate camera exposure errors. An alternative worth noting is to use a large HDR dataset to produce training data—for example, the Google HDR+ dataset [12]. One drawback, however, is that this dataset is a composite of a varying number of smartphone captured raw-RGB images that were first aligned to a composite raw-RGB image. The target ground truth image is based on an HDR-to-LDR algorithm applied to this composite raw-RGB image [8, 12]. We opt instead to use the FiveK dataset as it starts with a single high-quality raw-RGB image and the ground truth result is generated by an expert photographer.

3 Our Dataset

To train our model, we need a large number of training images rendered with realistic over- and underexposure errors and corresponding properly exposed

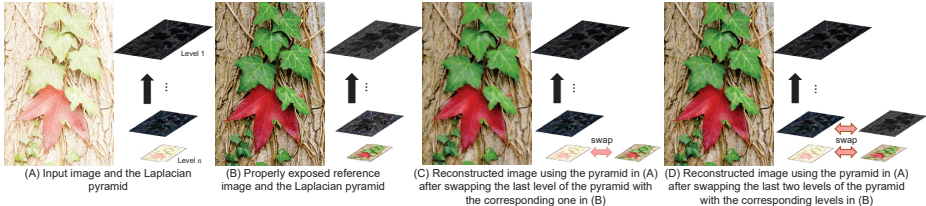


Fig. 3: Motivation behind our coarse-to-fine exposure correction approach. Example of an overexposed image and its corresponding properly exposed image shown in (A) and (B), respectively. The Laplacian pyramid decomposition allows us to enhance the color and detail information sequentially, as shown in (C) and (D), respectively.

ground truth images. As discussed in Sec. 2, such datasets are currently not publicly available. For this reason, our first task was to create a new dataset. Our dataset is rendered from the MIT-Adobe FiveK dataset [38], which has 5,000 raw-RGB images and corresponding sRGB images rendered manually by five expert photographers [38].

For each raw-RGB image, we use the Adobe Camera Raw SDK [39] to emulate different EVs as would be applied by a camera [40]. Adobe Camera Raw accurately emulates the nonlinear camera rendering procedures using metadata embedded in each DNG raw file [40, 41]. We render each raw-RGB image with different digital EVs to mimic real exposure errors. Specifically, we use the relative EVs -1.5 , -1 , $+0$, $+1$, and $+1.5$ to render images with underexposure errors, a zero gain of the original EV, and overexposure errors, respectively. The zero-gain relative EV is equivalent to the original exposure settings applied onboard the camera during capture time.

As the ground truth images, we use images that were manually retouched by an expert photographer (referred to as Expert C in [38]) as our target correctly exposed images, rather than using our rendered images with $+0$ relative EV. The reason behind this choice is that a significant number of images contain backlighting or partial exposure errors in the original exposure capture settings. The expert adjusted images were performed in ProPhoto RGB color space [38] (rather than raw-RGB), which we converted to a standard 8-bit sRGB color space encoding.

In total, we generated 24,330 8-bit sRGB images with different digital exposure settings. We discarded a small number of images that had misalignment with their corresponding ground truth image. These misalignments were due to different usage of the DNG crop area metadata by Adobe Camera Raw SDK and the expert. Our dataset is divided into three sets: (i) training set of 17,675 images, (ii) validation set of 750 images, and (iii) testing set of 5,905 images. The training, validation, and testing sets, use different images taken from the FiveK dataset. This means the training, validation, and testing images do not share any images in common. Fig. 2 shows examples of our generated 8-bit sRGB images and the corresponding properly exposed 8-bit sRGB reference images.

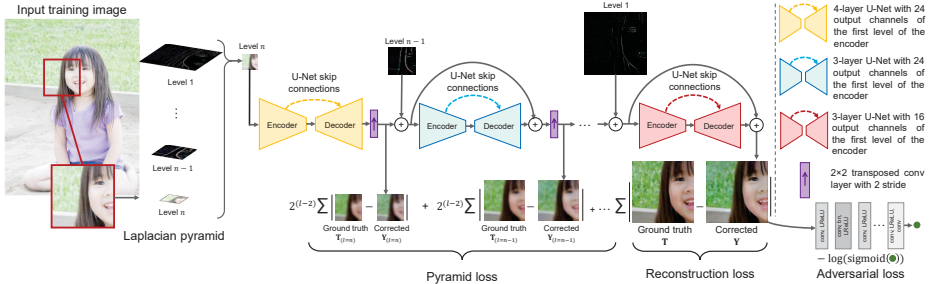


Fig. 4: Overview of our image exposure correction architecture. We propose a coarse-to-fine deep network to progressively correct exposure errors in 8-bit sRGB images. Our network first corrects the global color captured at the final level of the Laplacian pyramid and then the subsequent frequency layers.

4 Our Method

Given an 8-bit sRGB input image, \mathbf{I} , rendered with the incorrect exposure setting, our method aims to produce an output image, \mathbf{Y} , with fewer exposure errors than those in \mathbf{I} . As we target both over- and underexposed errors, our input image, \mathbf{I} , is expected to contain regions of nearly over- or under-saturated values with corrupted color and detail information. We propose to correct color and detail errors of \mathbf{I} in a sequential manner. Specifically, we propose to process a multi-resolution representation of \mathbf{I} , rather than directly dealing with the original form of \mathbf{I} . We use the Laplacian pyramid [42] as our multiresolution decomposition, which is derived from the Gaussian pyramid of \mathbf{I} .

4.1 Coarse-to-Fine Exposure Correction

Let \mathbf{X} represent the Laplacian pyramid of \mathbf{I} with n levels, such that $\mathbf{X}_{(l)}$ is the l^{th} level of \mathbf{X} . The last level of this pyramid (i.e., $\mathbf{X}_{(n)}$) captures low-frequency information of \mathbf{I} , while the first level (i.e., $\mathbf{X}_{(1)}$) captures the high-frequency information. Such frequency levels can be categorized into: (i) global color information of \mathbf{I} stored in the low-frequency level and (ii) image coarse-to-fine details stored in the mid- and high-frequency levels. These levels can be later used to reconstruct the full-color image \mathbf{I} .

Fig. 3 motivates our coarse-to-fine approach to exposure correction. Figs. 3-(A) and (B) show an example overexposed image and its corresponding well-exposed target, respectively. As observed, a significant exposure correction can be obtained by using only the low-frequency layer (i.e., the global color information) of the target image in the Laplacian pyramid reconstruction process, as shown in Fig. 3-(C). We can then improve the final image by enhancing the details in a sequential way by correcting each level of the Laplacian pyramid, as shown in Fig. 3-(D). Practically, we do not have access to the properly exposed image in Fig. 3-(B) at the inference stage, and thus our goal is to predict the missing color/detail information of each level in the Laplacian pyramid.

Inspired by this observation and the success of coarse-to-fine architectures for various other computer vision tasks (e.g., [43–46]), we design a DNN that corrects the global color and detail information of \mathbf{I} in a sequential manner using the Laplacian pyramid decomposition. The remaining part of this section explains the technical details of our model (Sec. 4.2), including details of the losses (Sec. 4.3), implementation and training (Sec. 4.4), and inference phase (Sec. 4.5).

4.2 Coarse-to-Fine Network

Our image exposure correction architecture sequentially processes the n -level Laplacian pyramid \mathbf{X} of image \mathbf{I} to produce the final corrected image \mathbf{Y} . The proposed model consists of n sub-networks. Each of these sub-networks is a U-Net-like architecture [47] with untied weights. We allocate the network capacity in the form of weights based on how significantly each sub-problem (i.e., global color correction and detail enhancement) contributes to our final result. Fig. 4 provides an overview of our network. As shown, the largest (in terms of weights) sub-network in our architecture is dedicated to processing the global color information in \mathbf{I} (i.e., $\mathbf{X}_{(n)}$). This sub-network (shown in yellow in Fig. 4) processes the low-frequency level $\mathbf{X}_{(n)}$ and produces an upscaled image $\mathbf{Y}_{(n)}$. The upscaling process scales up the output of our sub-network by a factor of two using strided transposed convolution with trainable weights. Next, we add the first mid-frequency level $\mathbf{X}_{(n-1)}$ to $\mathbf{Y}_{(n)}$ to be processed by the second sub-network in our model. This sub-network enhances the corresponding details of the current level and produces a residual layer that is then added to $\mathbf{Y}_{(n)} + \mathbf{X}_{(n-1)}$ to reconstruct image $\mathbf{Y}_{(n-1)}$, which is equivalent to the corresponding Gaussian pyramid level $n-1$. This refinement-upsampling process proceeds until the final output image, \mathbf{Y} , is produced. Our network is fully differentiable and thus can be trained in an end-to-end manner.

4.3 Losses

We train our model end-to-end to minimize the following loss function:

$$\mathcal{L} = \mathcal{L}_{\text{rec}} + \mathcal{L}_{\text{pyr}} + \mathcal{L}_{\text{adv}}, \quad (1)$$

where \mathcal{L}_{rec} denotes the reconstruction loss, \mathcal{L}_{pyr} the pyramid loss, and \mathcal{L}_{adv} the adversarial loss.

Reconstruction Loss: We use the L_1 loss function between the reconstructed and properly exposed reference images. This loss can be expressed as follows:

$$\mathcal{L}_{\text{rec}} = \sum_{p=1}^{3hw} |\mathbf{Y}(p) - \mathbf{T}(p)|, \quad (2)$$

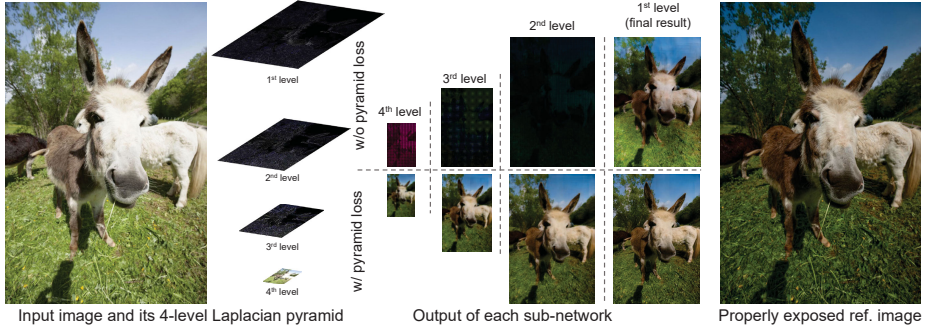


Fig. 5: Multiscale losses. Shown are the output of each sub-net trained with and without the pyramid loss (Eq. 3).

where h and w denote the height and width of the training image, respectively, and p is the index of each pixel in our corrected image, \mathbf{Y} , and the corresponding properly exposed reference image, \mathbf{T} , respectively. The individual losses are described below.

Pyramid Loss: To guide each sub-network to follow the Laplacian pyramid reconstruction procedure, we introduce dedicated losses at each pyramid level. Let $\mathbf{T}_{(l)}$ denote the l^{th} level of the Gaussian pyramid of our reference image, \mathbf{T} , after upsampling by a factor of two. We use a simple interpolation process for the upsampling operation [27]. Our pyramid loss is computed as follows:

$$\mathcal{L}_{\text{pyr}} = \sum_{l=2}^n 2^{(l-2)} \sum_{p=1}^{3h_l w_l} |\mathbf{Y}_{(l)}(p) - \mathbf{T}_{(l)}(p)|, \quad (3)$$

where h_l and w_l are twice the height and width of the l^{th} level in the Laplacian pyramid of the training image, respectively, and p is the index of each pixel in our corrected image at the l^{th} level $\mathbf{Y}_{(l)}$ and the properly exposed reference image at the same level $\mathbf{T}_{(l)}$, respectively. The pyramid loss not only gives a principled interpretation of the task of each sub-network but also results in less visual artifacts compared to training using only the reconstruction loss (see Fig. 5). Notice that without their intermediate pyramid losses, the multi-scale reconstructions deviate widely from the intermediate Gaussian targets.

Adversarial Loss: To perceptually enhance the reconstruction of the corrected image output in terms of realism and appeal, we also consider an adversarial loss as a regularizer. This adversarial loss term can be described by the following equation [48]:

$$\mathcal{L}_{\text{adv}} = -3hwn \log (\mathcal{S}(\mathcal{D}(\mathbf{Y}))), \quad (4)$$

where \mathcal{S} is the sigmoid function and \mathcal{D} is a discriminator DNN that is trained together with our main network.

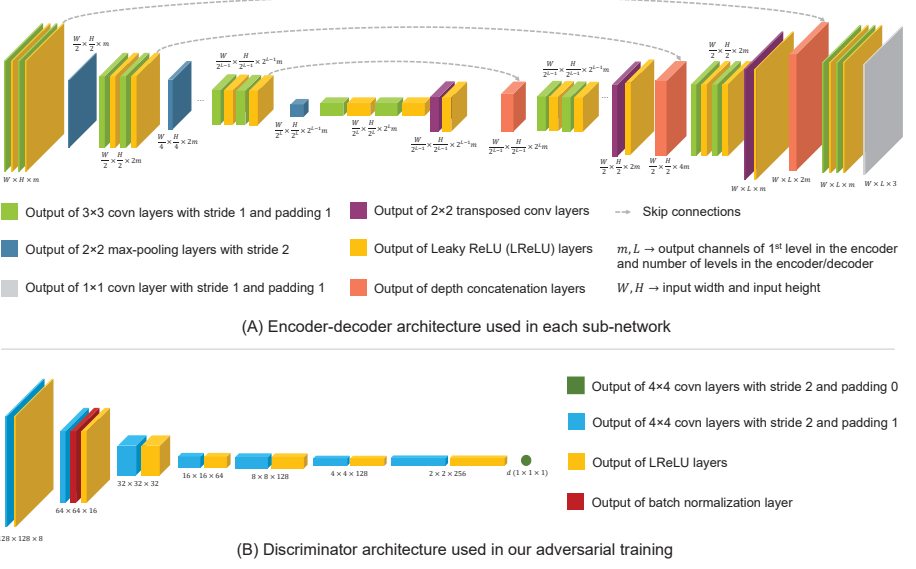


Fig. 6: Details of the architectures used in our work. (A) Encoder-decoder architecture [47] used to design our sub-networks in the main network. (B) Discriminator architecture.

4.4 Implementation and Training Details

In our implementation, we use a Laplacian pyramid with four levels (i.e., $n = 4$) and thus we have four sub-networks in our model. We provide the implementation details of our network, the discriminator network used in the adversarial training process, and the training details below.

4.4.1 Main Network Our main network consists of four sub-networks with $\sim 7M$ parameters trained in an end-to-end manner. Each sub-network accepts a different representation of the input image extracted from the Laplacian pyramid decomposition. The first sub-network is a four-layer encoder-decoder network with skip connections (i.e., U-Net-like architecture [47]). The output of the first convolutional (conv) layer has 24 channels. Our first sub-network has $\sim 4.4M$ learnable parameters and it accepts the low-frequency band level of the Laplacian pyramid, i.e., $\mathbf{X}_{(4)}$. The result of the first sub-network is then upscaled using a $2 \times 2 \times 3$ transposed conv layer with three output channels and a stride of two. This processed layer is then added to the first mid-frequency band level of the Laplacian pyramid (i.e., $\mathbf{X}_{(3)}$) and is fed to the second sub-network.

The second sub-network is a three-layer encoder-decoder network with skip connections. It has 24 channels in the first conv layer of the encoder, with a total of $\sim 1.1M$ learnable parameters. The second sub-network processes the upscaled input from the first sub-network and outputs a residual layer, which is then added back to the input to the second sub-network followed by a $2 \times 2 \times 3$ transposed conv layer with three output channels and a stride of two. The result is added to

the second mid-frequency band level of the Laplacian pyramid (i.e., $\mathbf{X}_{(2)}$) and is fed to the third sub-network, which generates a new residual that is added back again to the input of this sub-network.

The third sub-network has the same design as the second network. Finally, the result is added to the high-frequency band level of the Laplacian pyramid (i.e., $\mathbf{X}_{(1)}$) and is fed to the fourth sub-network to produce the final processed image.

The final sub-network is a three-layer encoder-decoder network with skip connections and has $\sim 482.2K$ learnable parameters, where the output of the first conv layer in its encoder has 16 channels. We provide the details of the main encoder-decoder architecture of each sub-network in Fig. 6-(A).

4.4.2 Discriminator Network In the adversarial training of our network, we use a light-weight discriminator network with $\sim 1M$ learnable parameters. We provide the details of the discriminator in Fig. 6-(B). Notice that unlike our main network, we resize all input image patches to have 256×256 pixels before being processed by the discriminator. The output of the last layer in our discriminator is a single scalar value which is then used in our loss during the optimization.

4.4.3 Training Details We use He et al.’s method [49] to initialize the weights of our encoder and decoder conv layers, while the bias terms are initialized to zero. We minimize our loss functions using the Adam optimizer [50] with a decay rate $\beta_1 = 0.9$ for the exponential moving averages of the gradient and a decay rate $\beta_2 = 0.999$ for the squared gradient. We use a learning rate of 10^{-4} to update the parameters of our main network and a learning rate of 10^{-5} to update our discriminator’s parameters.

We train our network on patches with different dimensions. Training begins without the adversarial loss, \mathcal{L}_{adv} , then \mathcal{L}_{adv} is added to enhance the results of our initial training [51]. Specifically, we begin our training without \mathcal{L}_{adv} on 176,590 patches with dimensions of 128×128 pixels extracted randomly from our training images for 40 epochs. The mini-batch size is set to 32. The learning rate is decayed by a factor of 0.5 after the first 20 epochs. Then, we continue training on another 105,845 patches with dimensions of 256×256 pixels for 30 epochs with a mini-batch size of eight. At this stage, we train our main network without \mathcal{L}_{adv} for 15 epochs and continue training for another 15 epochs with \mathcal{L}_{adv} . The learning rates for the main network and the discriminator network are decayed by a factor of 0.5 every 10 epochs. Finally, we fine-tune the trained networks on another 69,515 training patches with dimensions of 512×512 pixels for 20 epochs with a mini-batch size of four and a learning rate decay of 0.5 applied every five epochs.

We discard any training patches that have an average intensity less than 0.02 or higher than 0.98. We also discard homogeneous patches that have a gradient magnitude less than 0.06. We randomly left-right flip training patches for data augmentation.

In the adversarial training, we optimize both the main network and the discriminator in an iterative manner. At each optimization step, the learnable parameters of each network are updated to minimize its own loss function. The discriminator is trained to minimize the following loss function [48]:

$$\mathcal{L}_{\text{dsc}} = r(\mathbf{T}) + c(\mathbf{Y}), \quad (5)$$

where $r(\mathbf{T})$ refers to the discriminator loss of recognizing the properly exposed reference image \mathbf{T} , while $c(\mathbf{Y})$ refers to the discriminator loss of recognizing our corrected image \mathbf{Y} . The $r(\mathbf{T})$ and $c(\mathbf{Y})$ loss functions are given by the following equations:

$$r(\mathbf{T}) = -\log(\mathcal{S}(\mathcal{D}(\mathbf{T}))), \quad (6)$$

$$c(\mathbf{Y}) = -\log(1 - \mathcal{S}(\mathcal{D}(\mathbf{Y}))). \quad (7)$$

4.5 Inference Stage

Our network is fully convolutional and can process input images with different resolutions. While our model requires a reasonable memory size ($\sim 7\text{M}$ parameters), processing high-resolution images requires a high computational power that may not always be available. Furthermore, processing images with considerably higher resolution (e.g., 16-megapixel) than the range of resolutions used in the training process can affect our model's robustness with large homogeneous image regions. This issue arises because our network was trained on a certain range of effective receptive fields, which is very low compared to the receptive fields required for images with very high resolution. To that end, we use the bilateral guided upsampling method [52] to process high-resolution images. First, we resize the input test image to have a maximum dimension of 512 pixels. Then, we process the downsampled version of the input image using our model, followed by applying the fast upsampling technique [52] with a bilateral grid of $22 \times 22 \times 8$ cells. This process allows us to process a 16-megapixel image in ~ 4.5 seconds on average. This time includes ~ 0.5 seconds to run our network on an NVIDIA® GeForce GTX 1080™ GPU and ~ 4 seconds on an Intel® Xeon® E5-1607 @ 3.10 GHz machine for the guided upsampling process. Note the runtime of guided upsampling step can be significantly improved with a Halide implementation [53].

5 Empirical Evaluation

We compare our method against several existing methods for exposure correction and image enhancement. We first present quantitative results and comparisons in Sec. 5.1, followed by qualitative comparisons in Sec. 5.2. Finally, we present ablation studies performed to validate our architecture and loss function in Sec. 5.3.



Fig. 7: We evaluate the results of input images against all five expert photographers’ edits from the FiveK dataset [38].

5.1 Quantitative Results

To evaluate our method, we use our test set, which consists of 5,905 images rendered with different exposure settings, as described in Sec. 3. Specifically, our test set includes 3,543 well-exposed/overexposed images rendered with $+0$, $+1$, and $+1.5$ relative EVs, and 2,362 underexposed images rendered with -1 and -1.5 relative EVs.

We adopt the following three standard metrics to evaluate the pixel-wise accuracy and the perceptual quality of our results: (i) peak signal-to-noise ratio (PSNR), (ii) structural similarity index measure (SSIM) [54], and (iii) perceptual index (PI) [55]. The PI is given by:

$$\text{PI} = 0.5(10 - \text{Ma} + \text{NIQE}), \quad (8)$$

where both **Ma** [56] and **NIQE** [57] are *no-reference* image quality metrics.

For the pixel-wise error metrics – namely, PSNR and SSIM – we compare the results not only against the properly exposed rendered images by Expert C but also with *all* five expert photographers in the MIT-Adobe FiveK dataset [38]. Though the expert photographers may render the same image in different ways due to differences in the camera-based rendering settings (e.g., white balance, tone mapping), a common characteristic over all rendered images by the expert photographers is that they all have fairly proper exposure settings [38] (see Fig. 7). For this reason, we evaluate our method against the *five* expert rendered images as they all represent satisfactory exposed reference images.

We also evaluate a variety of previous non-learning and learning-based methods on our test set for comparison: histogram equalization (HE) [14], contrast-limited adaptive histogram equalization (CLAHE) [16], the weighted variational model (WVM) [59], the low-light image enhancement method (LIME) [3, 60], HDR CNN [30], DPED models [35], deep photo enhancer (DPE) models [9], the high-quality exposure correction method (HQEC) [4], RetinexNet [5], and deep underexposed photo enhancer (UPE) [7]. To render the reconstructed HDR images generated by the HDR CNN method [30] back into LDR, we tested both the deep reciprocating HDR transformation method (RHT) [34] and Adobe Photoshop’s (PS) HDR tool [58].

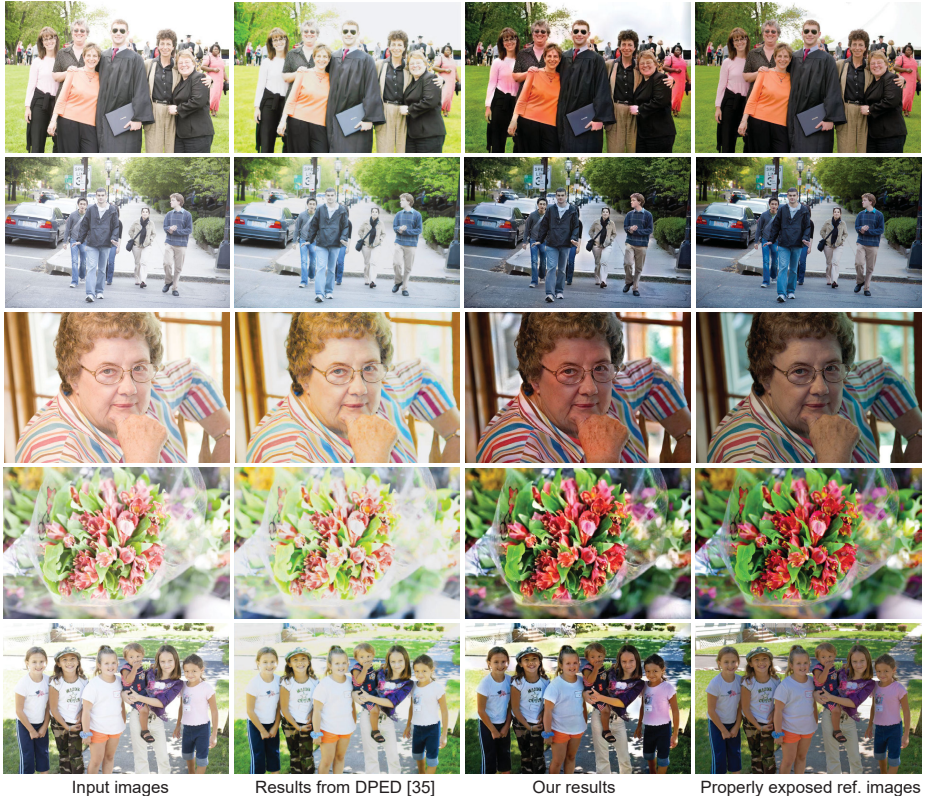


Fig. 8: Qualitative results of correcting overexposed images. Shown are the input images, results from the DPED [35], our results, and the corresponding ground truth images.

Table 1 summarizes the quantitative results obtained by each method. As shown in the top portion of the table, our method achieves the best results for overexposed images under all metrics. In the underexposed image correction setting, our results (middle portion of table) are on par with the state-of-the-art methods. Finally, in contrast to most of the existing methods, the results in the bottom portion of the table show that our method can effectively deal with *both* types of exposure errors.

For completeness, we further evaluate our method on the following standard image datasets used by previous low-light image enhancement methods: (i) LIME (10 images) [3], (ii) NPE (75 images) [24], (iii) VV (24 images) [61], and DICM (44 images) [62]. Similar to previous methods, we use the NIQE perceptual score [57] for evaluation. Table 2 compares results by our method and the following methods: LIME [3, 60], WVM [59], RetinexNet (RNet) [5], “kindling the darkness” method (KinD) [6], enlighten GAN (EGAN) [63], and deep bright-channel prior (BCP) [64]. As can be seen in Table 2, our method generally achieves perceptually superior results in correcting low-light 8-bit images.

Method	Expert A		Expert B		Expert C		Expert D		Expert E		Avg.		PI
	PSNR	SSIM											
+0, +1, and +1.5 relative EVs (3,543 properly exposed and overexposed images)													
HE [14] *	16.140	0.686	16.277	0.672	16.531	0.699	16.643	0.669	17.321	0.691	16.582	0.683	2.351
CLAHE [16] *	13.934	0.568	14.689	0.586	14.453	0.584	15.116	0.593	15.850	0.612	14.808	0.589	2.270
WVM [59] *	12.355	0.624	13.147	0.656	12.748	0.645	14.059	0.669	15.207	0.690	13.503	0.657	2.342
LIME [3, 60] *	09.627	0.549	10.096	0.569	9.875	0.570	10.936	0.597	11.903	0.626	10.487	0.582	2.412
HDR CNN [30] w/ RHT [34]	13.151	0.475	13.637	0.478	13.622	0.497	14.177	0.479	14.625	0.503	13.842	0.486	4.284
HDR CNN [30] w/ PS [58]	14.804	0.651	15.622	0.689	15.348	0.670	16.583	0.685	18.022	0.703	16.076	0.680	2.248
DPED (iPhone) [35]	12.680	0.562	13.422	0.586	13.135	0.581	14.477	0.596	15.702	0.630	13.883	0.591	2.909
DPED (BlackBerry) [35]	15.170	0.621	16.193	0.691	15.781	0.642	17.042	0.677	18.035	0.678	16.444	0.662	2.518
DPED (Sony) [35]	16.398	0.672	17.679	0.707	17.378	0.697	17.997	0.685	18.685	0.700	17.627	0.692	2.740
DPE (HDR) [9]	14.399	0.572	15.219	0.573	15.091	0.593	15.692	0.581	16.640	0.626	15.408	0.589	2.417
DPE (U-FiveK) [9]	14.314	0.615	14.958	0.628	15.075	0.645	15.987	0.647	16.931	0.667	15.453	0.640	2.630
DPE (S-FiveK) [9]	14.786	0.638	15.519	0.649	15.625	0.668	16.586	0.664	17.661	0.684	16.035	0.661	2.621
HQEC [4] *	11.775	0.607	12.536	0.631	12.127	0.627	13.424	0.652	14.511	0.675	12.875	0.638	2.387
RetinexNet [5]	10.149	0.570	10.880	0.586	10.471	0.595	11.498	0.613	12.295	0.635	11.059	0.600	2.933
Deep UPE [7]	10.047	0.532	10.462	0.568	10.307	0.557	11.583	0.591	12.639	0.619	11.008	0.573	2.428
Our method w/o \mathcal{L}_{adv}	18.976	0.743	19.767	0.731	19.980	0.768	18.966	0.716	19.056	0.727	19.349	0.737	2.189
Our method w/ \mathcal{L}_{adv}	18.874	0.738	19.569	0.718	19.788	0.760	18.823	0.705	18.936	0.719	19.198	0.728	2.183
-1 and -1.5 relative EVs (2,362 underexposed images)													
HE [14] *	16.158	0.683	16.293	0.669	16.517	0.692	16.632	0.665	17.280	0.684	16.576	0.679	2.486
CLAHE [16] *	16.310	0.619	17.140	0.646	16.779	0.621	15.955	0.613	15.568	0.608	16.350	0.621	2.387
WVM [59] *	17.686	0.728	19.787	0.764	18.670	0.728	18.568	0.729	18.362	0.724	18.615	0.735	2.525
LIME [3, 60] *	13.444	0.653	14.426	0.672	13.980	0.663	15.190	0.673	16.177	0.694	14.643	0.671	2.462
HDR CNN [30] w/ RHT [34]	14.547	0.456	14.347	0.427	14.068	0.441	13.025	0.398	11.957	0.379	13.589	0.420	5.072
HDR CNN [30] w/ PS [58]	17.324	0.692	18.992	0.714	18.047	0.696	18.377	0.689	19.593	0.701	18.467	0.698	2.294
DPED (iPhone) [35]	18.814	0.680	21.129	0.712	20.064	0.683	19.711	0.675	19.574	0.676	19.858	0.685	2.894
DPED (BlackBerry) [35]	19.519	0.673	22.333	0.745	20.342	0.669	19.611	0.683	18.489	0.653	20.059	0.685	2.633
DPED (Sony) [35]	18.952	0.679	20.072	0.691	18.982	0.662	17.450	0.629	15.857	0.601	18.263	0.652	2.905
DPE (HDR) [9]	17.625	0.675	18.542	0.705	18.127	0.677	16.831	0.665	15.891	0.643	17.403	0.673	2.340
DPE (U-FiveK) [9]	19.130	0.700	19.574	0.674	19.479	0.711	17.924	0.665	16.370	0.625	18.495	0.677	2.571
DPE (S-FiveK) [9]	20.153	0.738	20.973	0.697	20.915	0.738	19.050	0.688	17.510	0.648	19.720	0.702	2.564
HQEC [4] *	15.801	0.692	17.371	0.718	16.587	0.700	17.090	0.700	17.675	0.716	16.905	0.706	2.532
RetinexNet [5]	11.676	0.607	12.711	0.611	12.132	0.621	12.720	0.618	13.233	0.637	12.494	0.619	3.362
Deep UPE [7]	17.832	0.728	19.059	0.754	18.763	0.745	19.641	0.737	20.237	0.740	19.106	0.741	2.371
Our method w/o \mathcal{L}_{adv}	19.432	0.750	20.590	0.739	20.542	0.770	18.989	0.723	18.874	0.727	19.685	0.742	2.344
Our method w/ \mathcal{L}_{adv}	19.475	0.751	20.546	0.730	20.518	0.768	18.935	0.715	17.856	0.719	19.646	0.737	2.342
Combined over and underexposed images (5,905 images)													
HE [14] *	16.148	0.685	16.283	0.671	16.525	0.696	16.639	0.668	17.305	0.688	16.580	0.682	2.405
CLAHE [16] *	14.884	0.589	15.669	0.610	15.383	0.599	15.452	0.601	15.737	0.610	15.425	0.602	2.317
WVM [59] *	14.488	0.665	15.803	0.699	15.117	0.678	15.863	0.693	16.469	0.704	15.548	0.688	2.415
LIME [3, 60]	11.154	0.591	11.828	0.610	11.517	0.607	12.638	0.628	13.613	0.653	12.150	0.618	2.432
HDR CNN [30] w/ RHT [34]	13.709	0.467	13.921	0.458	13.800	0.474	13.716	0.446	13.558	0.454	13.741	0.460	4.599
HDR CNN [30] w/ PS [58]	15.812	0.667	16.970	0.699	16.428	0.681	17.301	0.687	18.650	0.702	17.032	0.687	2.267
DPED (iPhone) [35]	15.134	0.609	16.505	0.636	15.907	0.622	16.571	0.627	17.251	0.649	16.274	0.629	2.903
DPED (BlackBerry) [35]	16.910	0.642	18.649	0.713	17.606	0.653	18.070	0.679	18.217	0.668	17.890	0.671	2.564
DPED (Sony) [35]	17.419	0.675	18.636	0.701	18.020	0.683	17.554	0.660	17.778	0.663	17.881	0.676	2.806
DPE (HDR) [9]	15.690	0.614	16.548	0.626	16.305	0.626	16.147	0.615	16.341	0.633	16.206	0.623	2.417
DPE (U-FiveK) [9]	16.240	0.653	16.805	0.646	16.837	0.671	16.762	0.654	16.707	0.650	16.670	0.655	2.606
DPE (S-FiveK) [9]	16.933	0.678	17.701	0.668	17.744	0.696	17.572	0.674	17.601	0.670	17.510	0.677	2.621
HQEC [4] *	13.385	0.641	14.470	0.666	13.911	0.656	14.891	0.674	15.777	0.692	14.487	0.666	2.445
RetinexNet [5]	10.759	0.585	11.613	0.596	11.135	0.605	11.987	0.615	12.671	0.636	11.633	0.607	3.105
Deep UPE [7]	13.161	0.610	13.901	0.642	13.689	0.632	14.806	0.649	15.678	0.667	14.247	0.640	2.405
Our method w/o \mathcal{L}_{adv}	19.158	0.746	20.096	0.734	20.205	0.769	18.975	0.719	18.983	0.727	19.483	0.739	2.251
Our method w/ \mathcal{L}_{adv}	19.114	0.743	19.960	0.723	20.080	0.763	18.868	0.709	18.864	0.719	19.377	0.731	2.247

Table 1: Quantitative evaluation on our introduced test set. **The best results are highlighted with green and bold. The second- and third-best results are highlighted in yellow and red, respectively.** We compare each method with properly exposed reference image sets rendered by five expert photographers [38]. For each method, we present peak signal-to-noise ratio (PSNR), structural similarity index measure (SSIM) [54], and perceptual index (PI) [55]. We denote methods designed for underexposure correction in gray. Non-deep learning methods are marked by *. The terms U and S stand for unsupervised and supervised, respectively. Notice that higher PSNR and SSIM values are better, while lower PI values indicate better perceptual quality.

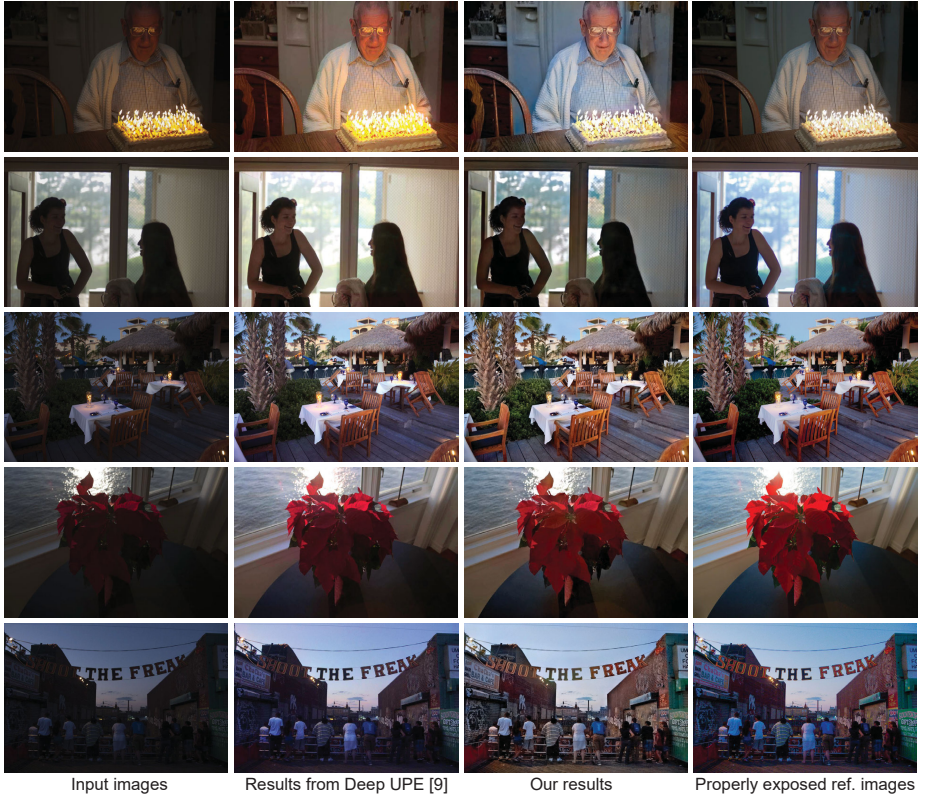


Fig. 9: Qualitative results of correcting underexposed images. Shown are the input images, results from the Deep UPE [9], our results, and the corresponding ground truth images.

5.2 Qualitative Results

We compare our method qualitatively with a variety of previous methods. Note we show results using the model trained with the adversarial loss term, as it produces perceptually superior results (see the perceptual metric results in Tables 1 and 2).

Figs. 8 and 9 show our results on different overexposed and underexposed images, respectively. As shown, our method provides compelling results for both exposure errors. We also compare our method with the most recent method for overexposure correction [26] in Fig. 10 – the source code of [26] is not yet



Fig. 10: Qualitative comparison with HDR CNN [30] and Zhang et al. [26].

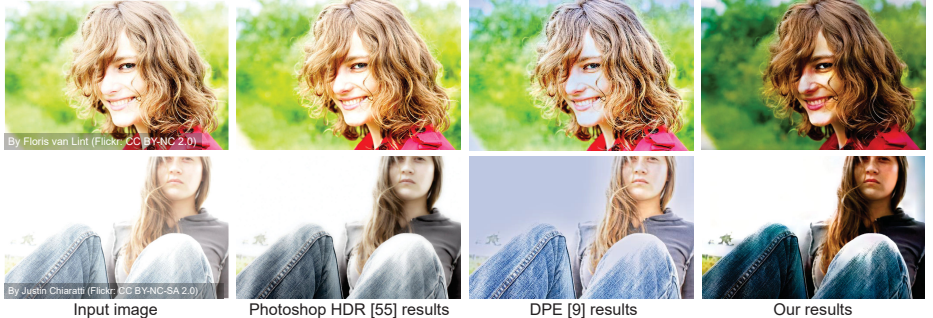


Fig. 11: Qualitative comparison with Adobe Photoshop’s local adaptation HDR function [58] and DPE [9]. Input images are taken from Flickr.

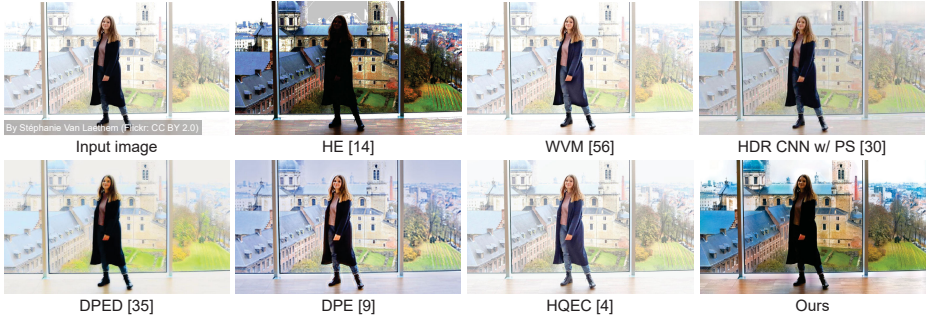


Fig. 12: Qualitative comparison with several existing methods in correcting partially overexposed regions due to backlighting. Input image is from Flickr.

available; the result is taken directly from the original paper [26]. As shown, our results are arguably visually superior to the other methods, even when input images have hard backlight conditions, as shown in the second row in Fig. 9 and the example in Fig. 12.

We also ran our model on several images from Flickr that are outside our introduced dataset, as shown in Figs. 1, 11, and 12. As with the images from our proposed dataset, our results on the Flickr images are arguably superior to the compared methods.

Our method produces unsatisfactory results in regions that have insufficient semantic information, as shown in Fig. 13. For example, the input image shown in the first row in Fig. 13 is completely saturated and contains almost no details in the region of the man’s face. We can see that our network cannot constrain the color inside the face region due to the lack of semantic information. It also can be observed that our method may introduce noise when the input image has very dark regions, as shown in the second example in Fig. 13. These challenging conditions prove difficult for other methods as well.

Image set	NPE [24]	LIME [3]	WVM [59]	RNet [5]	KinD [6]	EGAN [63]	DBCP [64]	Ours w/o \mathcal{L}_{adv}	Ours w/ \mathcal{L}_{adv}
LIME [3]	3.91	4.16	3.79	4.42	3.72	3.72	3.78	3.76	3.76
NPE [24]	3.95	4.26	3.99	4.49	3.88	4.11	3.18	3.20	3.18
VV set [61]	2.52	2.49	2.85	2.60	-	2.58	-	2.28	2.28
DICM [62]	3.76	3.85	3.90	4.20	-	-	3.57	2.55	2.50
Avg.	3.54	3.69	3.63	3.93	3.80	3.50	3.48	2.95	2.93

Table 2: Perceptual quality evaluation. Summary of NIQE scores [57] on different *low-light* image datasets. Highlights are in the same format as Table 1.

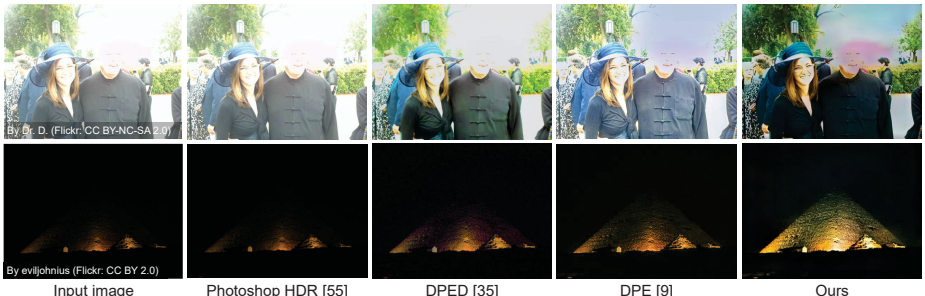


Fig. 13: Failure examples of correcting (top) overexposed and (bottom) underexposed images. The input images are taken from Flickr.

5.3 Ablation Studies

This section presents details on the ablation studies that were performed to validate the architecture and loss function.

5.3.1 Loss Function Our loss function in Eq. 1 includes three main terms. The first term is the standard reconstruction loss (i.e., L_1 loss). The second and third terms consist of the pyramid and adversarial losses, respectively, which are introduced to further improve the reconstruction and perceptual quality of the output images. In the following part of this section, we discuss the effect of these loss terms.

Pyramid Loss Impact In Fig. 5, we show the output of each sub-network when we train our model with and without the pyramid loss. We observe that the pyramid loss helps to provide additional supervision to guide each sub-network to follow a coarse-to-fine reconstruction. In this ablation study, we aim to quantitatively evaluate the effect of the pyramid loss on our final results.

We train two light-weight models of our main network with and without our pyramid loss term. Each model has four 3-layer U-Nets with a total of $\sim 4M$ learnable parameters, where the number of output channels of the first encoder in each U-Net is set to 24.

The training is performed on a sub-set of our training data for $\sim 150,000$ iterations on $80,000$ 128×128 patches, $\sim 100,000$ iterations on $40,000$ 256×256 patches, and $\sim 25,000$ iterations on $25,000$ 512×512 patches. Table 3 shows the results on 500 randomly selected images from our validation set. The results

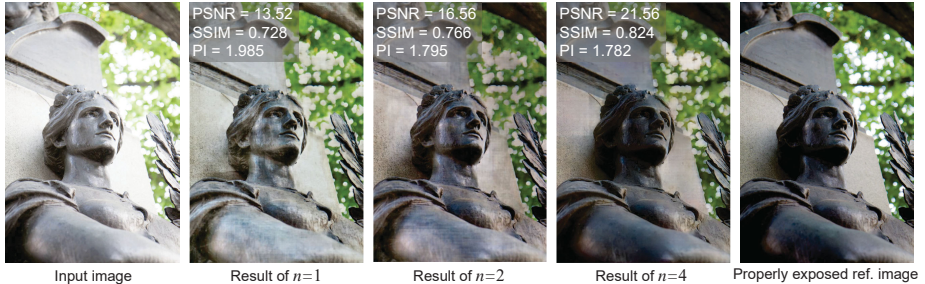


Fig. 14: Comparison of results by varying the number of Laplacian pyramid levels. Notice that higher PSNR and SSIM values are better, while lower PI values indicate better perceptual quality.

	Pyramid loss \mathcal{L}_{pyr}		Number of levels n		
	w/o	w/	$n = 1$	$n = 2$	$n = 4$
PSNR	18.041	18.385	16.984	17.442	18.385
SSIM	0.746	0.749	0.723	0.734	0.749

Table 3: Results of our ablation study on 500 images randomly selected from our validation set. We show the effects of: (i) the pyramid loss, \mathcal{L}_{pyr} , and (ii) the number of levels, n , in the main network. The best PSNR/SSIM values are indicated with bold for each experiment.

show that the pyramid loss not only helps in providing a better interpretation of the task of each sub-network but also improves the final results.

Adversarial Loss Impact In Tables 1 and 2, we show quantitative results of our method with and without the adversarial loss term. Our trained model with the adversarial loss term achieves better perceptual quality (i.e., lower PI values [55]) than training without the adversarial loss term.

Fig. 15 shows qualitative comparisons of our results with and without the adversarial loss. As shown, the network trained without the adversarial training tends to produce darker images and slightly unrealistic colors in some cases, while the adversarial regularization improves the perceptual quality of our results.

5.3.2 Number of Laplacian Pyramid Levels We repeat the same experimental setup described in Sec. 5.3.1 with a varying number of Laplacian pyramid levels (sub-networks). Specifically, we train a network with $n = 1$ levels—this network is equivalent to a vanilla U-Net-like architecture [47]. Additionally, we train another network with $n = 2$ (i.e., two sub-networks).

For a fair comparison, we fix the total number of parameters in each model by changing the number of filters in the conv layers. Specifically, we set the number of output channels of the first layer in the encoder to 48 for the trained model with $n = 1$, while we decrease it to 34 for the two-sub-net model (i.e., $n = 2$) to have approximately the same number of learnable parameters. Thus, the trained



Fig. 15: Comparisons between our results with (w/) and without (w/o) the adversarial loss for training. Notice that higher PSNR and SSIM values are better, while lower PI values indicate better perceptual quality.

model in Sec. 5.3.1 to study the pyramid loss impact and the additional two trained models have approximately the same number of parameters.

Table 3 shows the results obtained by each model on the same random validation image subset used to study the pyramid loss impact in Sec. 5.3.1. Fig. 14 shows a qualitative comparison. As can be seen, the best quantitative and qualitative results are obtained using the four-sub-net model (i.e., $n = 4$ levels).

6 Concluding Remarks

We proposed a coarse-to-fine deep learning model for overexposed and underexposed image correction. We employed the Laplacian pyramid decomposition to process input images in different frequency bands. Our method is designed to sequentially correct each of the Laplacian pyramid levels in a multi-scale manner, starting with the global color in the image and progressively addressing the image details. Our method is enabled by generating a large dataset of over 24,000 images rendered with different exposure errors. Each image in our introduced dataset has a reference image properly rendered by a well-trained photographer with well-exposure compensation. Through extensive evaluation, we showed that our method produces compelling results compared to available solutions for cor-

recting images rendered with exposure errors. We believe that our dataset will help future work on improving exposure correction for photographs.

References

- Peterson, B.: Understanding exposure: How to shoot great photographs with any camera. AmPhoto Books (2016)
- Karaimer, H.C., Brown, M.S.: A software platform for manipulating the camera imaging pipeline. In: ECCV. (2016)
- Guo, X., Li, Y., Ling, H.: LIME: Low-light image enhancement via illumination map estimation. *IEEE Transactions on Image Processing* **26**(2) (2017) 982–993
- Zhang, Q., Yuan, G., Xiao, C., Zhu, L., Zheng, W.S.: High-quality exposure correction of underexposed photos. In: ACM MM. (2018)
- Wei, C., Wang, W., Yang, W., Liu, J.: Deep retinex decomposition for low-light enhancement. In: BMVC. (2018)
- Zhang, Y., Zhang, J., Guo, X.: Kindling the darkness: A practical low-light image enhancer. In: ACM International Conference on Multimedia. (2019)
- Wang, R., Zhang, Q., Fu, C.W., Shen, X., Zheng, W.S., Jia, J.: Underexposed photo enhancement using deep illumination estimation. In: CVPR. (2019)
- Gharbi, M., Chen, J., Barron, J.T., Hasinoff, S.W., Durand, F.: Deep bilateral learning for real-time image enhancement. *ACM Transactions on Graphics (TOG)* **36**(4) (2017) 118:1–118:12
- Chen, Y.S., Wang, Y.C., Kao, M.H., Chuang, Y.Y.: Deep photo enhancer: Unpaired learning for image enhancement from photographs with GANs. In: CVPR. (2018)
- Chen, C., Chen, Q., Xu, J., Koltun, V.: Learning to see in the dark. In: CVPR. (2018)
- Hu, Y., He, H., Xu, C., Wang, B., Lin, S.: Exposure: A white-box photo post-processing framework. *ACM Transactions on Graphics (TOG)* **37**(2) (2018) 26:1–26:17
- Hasinoff, S.W., Sharlet, D., Geiss, R., Adams, A., Barron, J.T., Kainz, F., Chen, J., Levoy, M.: Burst photography for high dynamic range and low-light imaging on mobile cameras. *ACM Transactions on Graphics (TOG)* **35**(6) (2016) 1–12
- Liba, O., Murthy, K., Tsai, Y.T., Brooks, T., Xue, T., Karnad, N., He, Q., Barron, J.T., Sharlet, D., Geiss, R., Hasinoff, S.W., Pritch, Y., Levoy, M.: Handheld mobile photography in very low light. *ACM Transactions on Graphics (TOG)* **38**(6) (2019) 1–16
- Gonzalez, R.C., Woods, R.E.: *Digital Image Processing*. Addison-Wesley Longman Publishing Co., Inc. (2001)
- Pizer, S.M., Amburn, E.P., Austin, J.D., Cromartie, R., Geselowitz, A., Greer, T., ter Haar Romeny, B., Zimmerman, J.B., Zuiderveld, K.: Adaptive histogram equalization and its variations. *Computer Vision, Graphics, and Image Processing* **39**(3) (1987) 355–368
- Zuiderveld, K.: Contrast limited adaptive histogram equalization. In: *Graphics Gems IV*. (1994) 474–485
- Celik, T., Tjahjadi, T.: Contextual and variational contrast enhancement. *IEEE Transactions on Image Processing* **20**(12) (2011) 3431–3441
- Lee, C., Lee, C., Kim, C.S.: Contrast enhancement based on layered difference representation of 2D histograms. *IEEE Transactions on Image Processing* **22**(12) (2013) 5372–5384

19. Yuan, L., Sun, J.: Automatic exposure correction of consumer photographs. In: ECCV. (2012)
20. Yu, R., Liu, W., Zhang, Y., Qu, Z., Zhao, D., Zhang, B.: DeepExposure: Learning to expose photos with asynchronously reinforced adversarial learning. In: NeurIPS. (2018)
21. Park, J., Lee, J.Y., Yoo, D., So Kweon, I.: Distort-and-recover: Color enhancement using deep reinforcement learning. In: CVPR. (2018)
22. Land, E.H.: The retinex theory of color vision. *Scientific American* **237**(6) (1977) 108–129
23. Jobson, D.J., Rahman, Z., Woodell, G.A.: A multiscale retinex for bridging the gap between color images and the human observation of scenes. *IEEE Transactions on Image Processing* **6**(7) (1997) 965–976
24. Wang, S., Zheng, J., Hu, H.M., Li, B.: Naturalness preserved enhancement algorithm for non-uniform illumination images. *IEEE Transactions on Image Processing* **22**(9) (2013) 3538–3548
25. Meylan, L., Susstrunk, S.: High dynamic range image rendering with a retinex-based adaptive filter. *IEEE Transactions on Image Processing* **15**(9) (2006) 2820–2830
26. Zhang, Q., Nie, Y., Zheng, W.S.: Dual illumination estimation for robust exposure correction. In: Computer Graphics Forum. (2019)
27. Mertens, T., Kautz, J., Van Reeth, F.: Exposure fusion: A simple and practical alternative to high dynamic range photography. In: Computer Graphics Forum. (2009)
28. Kalantari, N.K., Ramamoorthi, R.: Deep high dynamic range imaging of dynamic scenes. *ACM Transactions on Graphics (TOG)* **36**(4) (2017) 144–1
29. Endo, Y., Kanamori, Y., Mitani, J.: Deep reverse tone mapping. *ACM Transactions on Graphics (TOG)* **36**(6) (2017) 177:1–177:10
30. Eilertsen, G., Kronander, J., Denes, G., Mantiuk, R., Unger, J.: HDR image reconstruction from a single exposure using deep CNNs. *ACM Transactions on Graphics (TOG)* **36**(6) (2017) 178:1–178:15
31. Moriwaki, K., Yoshihashi, R., Kawakami, R., You, S., Naemura, T.: Hybrid loss for learning single-image-based HDR reconstruction. *arXiv preprint arXiv:1812.07134* (2018)
32. Debevec, P.E., Malik, J.: Recovering high dynamic range radiance maps from photographs. In: ACM SIGGRAPH. (1997)
33. Cai, J., Gu, S., Zhang, L.: Learning a deep single image contrast enhancer from multi-exposure images. *IEEE Transactions on Image Processing* **27**(4) (2018) 2049–2062
34. Yang, X., Xu, K., Song, Y., Zhang, Q., Wei, X., Lau, R.W.: Image correction via deep reciprocating HDR transformation. In: CVPR. (2018)
35. Ignatov, A., Kobyshev, N., Timofte, R., Vanhoey, K., Van Gool, L.: DSLR-quality photos on mobile devices with deep convolutional networks. In: ICCV. (2017)
36. Ignatov, A., Kobyshev, N., Timofte, R., Vanhoey, K., Van Gool, L.: WESPE: Weakly supervised photo enhancer for digital cameras. In: CVPR Workshops. (2018)
37. Maaten, L.v.d., Hinton, G.: Visualizing data using t-SNE. *Journal of Machine Learning Research* **9** (2008) 2579–2605
38. Bychkovsky, V., Paris, S., Chan, E., Durand, F.: Learning photographic global tonal adjustment with a database of input / output image pairs. In: CVPR. (2011)
39. Adobe: Color and camera raw. <https://helpx.adobe.com/ca/photoshop-elements/using/color-camera-raw.html> Accessed: 2020-03-05.

40. Schewe, J., Fraser, B.: Real World Camera Raw with Adobe Photoshop CS5. Pearson Education (2010)
41. Afifi, M., Price, B., Cohen, S., Brown, M.S.: When color constancy goes wrong: Correcting improperly white-balanced images. In: CVPR. (2019)
42. Burt, P., Adelson, E.: The Laplacian pyramid as a compact image code. IEEE Transactions on Communications **31**(4) (1983) 532–540
43. Denton, E.L., Chintala, S., szlam, a., Fergus, R.: Deep generative image models using a Laplacian pyramid of adversarial networks. In: NeurIPS. (2015)
44. Shaham, T.R., Dekel, T., Michaeli, T.: SinGAN: Learning a generative model from a single natural image. In: ICCV. (2019)
45. Lai, W.S., Huang, J.B., Ahuja, N., Yang, M.H.: Deep Laplacian pyramid networks for fast and accurate super-resolution. In: CVPR. (2017)
46. Ma, R., Hu, H., Xing, S., Li, Z.: Efficient and fast real-world noisy image denoising by combining pyramid neural network and two-pathway unscented Kalman filter. IEEE Transactions on Image Processing **29**(1) (2020) 3927–3940
47. Ronneberger, O., Fischer, P., Brox, T.: U-Net: Convolutional networks for biomedical image segmentation. In: MCCAII. (2015)
48. Goodfellow, I., Pouget-Abadie, J., Mirza, M., Xu, B., Warde-Farley, D., Ozair, S., Courville, A., Bengio, Y.: Generative adversarial nets. In: NeurIPS. (2014)
49. He, K., Zhang, X., Ren, S., Sun, J.: Delving deep into rectifiers: Surpassing human-level performance on ImageNet classification. In: ICCV. (2015)
50. Kingma, D.P., Ba, J.: Adam: A method for stochastic optimization. arXiv preprint arXiv:1412.6980 (2014)
51. Ma, L., Jia, X., Sun, Q., Schiele, B., Tuytelaars, T., Van Gool, L.: Pose guided person image generation. In: NeurIPS. (2017)
52. Chen, J., Adams, A., Wadhwa, N., Hasinoff, S.W.: Bilateral guided upsampling. ACM Transactions on Graphics (TOG) **35**(6) (2016) 1–8
53. Ragan-Kelley, J., Barnes, C., Adams, A., Paris, S., Durand, F., Amarasinghe, S.: Halide: A language and compiler for optimizing parallelism, locality, and re-computation in image processing pipelines. In: ACM SIGPLAN Conference on Programming Language Design and Implementation. (2013)
54. Zhou Wang, Bovik, A.C., Sheikh, H.R., Simoncelli, E.P.: Image quality assessment: From error visibility to structural similarity. IEEE Transactions on Image Processing **13**(4) (2004) 600–612
55. Blau, Y., Mechrez, R., Timofte, R., Michaeli, T., Zelnik-Manor, L.: The 2018 PIRM challenge on perceptual image super-resolution. In: ECCV Workshops. (2018)
56. Ma, C., Yang, C.Y., Yang, X., Yang, M.H.: Learning a no-reference quality metric for single-image super-resolution. Computer Vision and Image Understanding **158** (2017) 1–16
57. Mittal, A., Soundararajan, R., Bovik, A.C.: Making a “completely blind” image quality analyzer. IEEE Signal Processing Letters **20**(3) (2012) 209–212
58. Dayley, L.D., Dayley, B.: Photoshop CS5 Bible. John Wiley & Sons (2010)
59. Fu, X., Zeng, D., Huang, Y., Zhang, X.P., Ding, X.: A weighted variational model for simultaneous reflectance and illumination estimation. In: CVPR. (2016)
60. Guo, X.: LIME: A method for low-light image enhancement. In: ACM MM. (2016)
61. Vonikakis, V.: Busting image enhancement and tone-mapping algorithms. <https://sites.google.com/site/vonikakis/datasets> Accessed: 2020-03-05.
62. Lee, C., Lee, C., Kim, C.S.: Contrast enhancement based on layered difference representation. In: ICIP. (2012)

63. Jiang, Y., Gong, X., Liu, D., Cheng, Y., Fang, C., Shen, X., Yang, J., Zhou, P., Wang, Z.: EnlightenGAN: Deep light enhancement without paired supervision. arXiv preprint arXiv:1906.06972 (2019)
64. Lee, H., Sohn, K., Min, D.: Unsupervised low-light image enhancement using bright channel prior. IEEE Signal Processing Letters **27** (2020) 251–255